Measuring Thermal and Electrical Performances of Additively Manufactured Magnetic Shielding Material: An Active Thermography Approach

Measuring Thermal and Electrical Performances of Additively Manufactured Magnetic Shielding Material: An Active Thermography Approach

Luca Santoro[a], Michele Quercio[b], Aldo Canova[b] and Raffaella Sesana[a]

[a]Mechanical and Aerospace Engineering Department, Politecnico di Torino, Torino, Italy; [b]Energy Department, Politecnico di Torino, Torino, Italy

ARTICLE HISTORY
Compiled April 22, 2024

ABSTRACT
The thermal and electrical responses of additive manufactured specimens were analyzed for a additive manufactured steel magnetic shield as a case study. The analysis was based on the evidence that variations in the thermal properties of a material can be measured as a phase delay in thermal diffusion through the material bulk. The signal post-processing was performed and the results were presented in a phase diagram. The results showed that after heat treatment, the slope of the phase diagram changed to less steep, indicating an increase in thermal diffusivity and hence, thermal conductivity. The electrical conductivity was predicted using the thermal conductivity and the Weidemann-Franz law and validated by experimental measurements of the electrical conductivity. The same approach was applied to predict the electrical conductivity in the magnetic shielding, taking into consideration the scaling of the density due to porosity. The results showed that the thermographic non destructive full field non contact approach can be used to evaluate the electrical properties of a component and that the heat-treated specimens show better thermal diffusivity and hence, thermal and electrical conductivity.

KEYWORDS
Active thermography; Additive manufacturing; Electrical properties; Wiedemann-Franz; Image processing; Non-contact measurement;

1. Introduction

Additive Manufacturing (AM) technologies are being widely used in the industrial sector for the production of high-performing and complex components [1–8]. The flexibility to produce components with intricate geometries and specific materials has increased their application in various industries, such as aerospace [9], trend [10], and other sectors [11]. Among the different AM techniques, Laser Powder Bed Fusion (LPBF) is the most commonly used [12,13]. The quality of the components produced using AM is related to various factors such as the process parameters (laser power, laser scanning path, and scan speed) and the orientation of the component on the printing platform [14,15]. Optimizing these factors helps in reducing the number of defects present in the components, both at the surface and sub-surface levels. The typical defects found in AM components include impurities, keyhole collapse, solidification

CONTACT Luca Santoro Author. Email: luca.santoro@polito.it

cracking, and surface-connected porosity [16]. These defects can be detected through either destructive or non-destructive testing methods. However, non-destructive testing is preferred due to the high production cost of AM [17]. Among the non-destructive defect detection methods, we can distinguish between in-line [18–20] and post-production tests [21–23]. Post-production testing techniques include active infrared thermography (aIRT), X-ray computed tomography (CT), and ultrasonic testing (UT) [24]. The powder material used in AM is subjected to heat treatments that alter its physical and mechanical properties. Hence, it is crucial to characterize the components properties after the manufacturing process. In literature, studies were conducted to investigate the effect of heat treatments on the electrical resistivity of AM materials [25]. However, as far as ferromagnetic materials are concerned, only magnetic properties were studied for different processes and different alloys [26–31]. The measurement of thermal properties of a material was the focus of intense research in recent years [32] , with many researchers focusing on active thermography techniques. Active thermography was used as a non-destructive testing method for several decades and it was used to characterize corrosion defects by means of a halogen lamp as the heat excitation source, as described in [33,34] presents an active thermography approach using a laser heat source coupled to a DMD 1024x768 mirror array, which enables the identification of hidden defects and their length measurement. [35] presents an analytical, numerical, and experimental study of the effect of thermal diffusivity and crack defects using the flying spot laser thermography technique, which involves introducing a moving laser heat source and performing a linear scan with constant velocity. [36] presents an approach to defect characterization in anisotropic materials using active thermography with a halogen lamp as the heat source, similarly [33]. In addition to halogen lamps, other excitation sources for active thermography include ultrasonic thermography [37,38], induction thermography [39–42] evaluates the thermal diffusivity between two different specimens of boron steel with different heat treatments using a pulsed laser spot active thermography approach. Physicians and material engineers use the lock-in thermography technique to characterize particular materials[43]. The main difficulty in this methodology consists in the sample preparation since the thermal measurement is sensitive to local emissivity, shape and internal properties (eg. anisotropy) of the tested material. In addition, the measurement needs a good setup, in [44] a vacuum jacket is used in order to avoid heat losses and nonlinearities due to convective phenomena, then different measurements are done by the use of a thermocouple and a movable specimen holder. In [45] the same method is used but on $200\mu m$ thick stripe-shaped samples. In [46] the lock-in method is used to measure anisotropic thermal diffusivity with respect to the fiber orientation, in this work it is specified that the thermal diffusion length parameter, and thus the frequency, are chosen in order to have an averaged measure through the thickness for the in-plane diffusivity. A more challenging application of the methodology is presented in [47] where the lock-in stimulation is applied on a transparent crystal, or in [48] another similar application on semitransparent thin films is presented. The shielding performance of magnetic materials is influenced by their permeability and electrical conductivity, as well as the thickness and shape of the shield [49–56]. Non-destructive control of the electrical properties can therefore improve the design and verification of magnetic shielding, especially when quality control is combined with property control [57–61]. Despite the importance of this topic, little literature exists on the evaluation of electric and magnetic properties. Some papers on magnetic shields produced using additive manufacturing (AM) using polymeric materials for high-frequency applications have been published [62–64], but few studies have focused on this area. In the present work,

the authors present the use of active thermography to derive the electrical properties of an electromagnetic shield made of Fe2.9%Si from measured thermal properties. The motivation behind this research is to establish a rapid, reliable, and non-destructive technique to measure and verify the shielding performance of magnetic shields, especially for laboratory equipment applications, with complex geometries which can be manufactured using AM. The proposed technique aims at evaluating electrical properties on the finished piece, properties which can be locally affected by due to the high level of complexity of the additive manufacturing process. To this aim, material characterization was performed on material samples and the obtained parameters were applied to estimate the electrical properties in the component.

1.1. Analytical background: the Wiedemann Franz formulation

The Wiedemann and Franz correlation [65] allows for linking thermal and electrical conductivity in bulk metallic materials. It is an empirical formulation reported in Eq.1 which relates the thermal diffusivity D to the electrical conductivity σ for bulk materials. This relation, if validated by means of thermographic thermal parameters calibration, allows the non destructive characterization of components, without laboratory measurements performed on dedicated samples, which is a critical issue when dealing with additive manufactured materials where process variables strongly affect physical and mechanical properties. This formulation was used in various works [66,67] to correlate the thermal phenomena with the electrical ones for the investigated materials. It was used for the first time on ferromagnetic samples produced by AM. The validation of the use of this technique combined with eq. 1 would lead to innovation in this sector. This would mean evaluating the electrical and thermal properties through non-destructive testing directly on the piece. This would reduce not only processing times but also processing costs.

$$L = \frac{K}{\sigma T} \tag{1}$$

Where L is the Lorentz number (2.44 3 *10e-8), T the temperature in Kelvin, K the thermal conductivity in J/mK, and σ the electrical conductivity

1.2. Analytical background: the Lock-in Method

The analytical formulation of the phenomena has been demonstrated many times. In [68], a complete demonstration is presented. The formulation considers the finite radius of the laser beam and the gaussian distribution of the laser heat source on a isotropic slab. The oscillating component of temperature equation in the Hankel space [68] T_{ac} is given by

$$\begin{aligned} T_{ac}(r,z) = \frac{P_0}{4\pi K}\int_0^{+\infty} \delta J_o(\delta r)\frac{e^{-(\delta a)^2/8}}{\beta} \\ \times\left[\frac{(1+H_1)e^{\beta(\ell+z)}+(1-H_1)e^{-\beta(\ell+z)}}{(1+H_0)(1+H_1)e^{\beta\ell}-(1-H_0)(1-H_1)e^{-\beta\ell}}\right]d\delta \end{aligned} \tag{2}$$

Where ℓ is the slab thickness, P_0 is the laser beam power with a Gaussian profile of radius a and a modulation frequency $f(\omega = 2\pi f$, δ is the Hankel variable, J_0 is the Bessel function of the zeroth order and $\beta^2 = \delta^2 + \sigma^2$, being $\sigma = \sqrt{i\omega/D}$ the thermal wave vector, $H_0 = h_0/K\beta$ and $H_1 = h_1/K\beta$ where K is the thermal conductivity and h_0 and h_1 are the heat transfer coefficient of respectively the upper and lower surfaces. Then the model is simplified, neglecting the heat conduction to the surrounding gas. Two case of interest are therefore presented.

If the slab is thermally thin, for example $\ell \ll \mu$, so with a thickness smaller then the thermal diffusion length, and accordingly to the hypothesis $e^{\pm\beta\ell} \approx 1 \pm \beta\ell$ and $h_0 \approx h_1 \approx h$ Then the equation 2 simplifies to:

$$T_{ac} = \frac{P_o}{4\pi K\ell}\int_0^{+\infty} \delta I_o(\delta r)\frac{e^{-(\delta a)^2/8}}{\beta'^2}d\delta \tag{3}$$

Where $\beta'^2 = \delta^2 = \sigma'^2$, with $\sigma'^2 = \sigma^2 + (2h/K\ell)$. In the *thermally thin slab* subcase the thermal distribution of oscillating temperature does not change along the thickness.

Then assuming a collimated laser beam (a=0) the equation 3 reduces to:

$$T_{ac}(r, a = 0) = \frac{P_o}{4\pi K\ell}K_o(\sigma' r) \tag{4}$$

Where K_0 is the zeroth order of the Kelvin function. Then using the asymptotic approach eq 4 reduces, for large r values, to:

$$\begin{aligned} T(r \to \infty, a = 0) &\approx \frac{P_o}{4\pi K\ell}\sqrt{\frac{\pi}{2\sigma'}}\frac{e^{-\sigma' r}}{\sqrt{r}} = \\ &= \frac{P_o}{4\pi K\ell}\sqrt{\frac{\pi}{2}}\frac{1}{\sqrt{\sigma'_R + i\sigma'_I}}\frac{e^{-\sigma'_R r}}{\sqrt{r}}e^{-i\sigma'_I r} \end{aligned} \tag{5}$$

Where σ'_R and σ'_l are the real and imaginary parts of σ'. From 5 derives the linear correlation between r and the phase's (Φ) slope $m_\Phi = -\sigma'_l$. Another important consideration derives from the fact that for finite laser spot size ($a \neq 0$) the amplitude or phase changes only nearby the spot, while if larger radii are used both slopes remain unchanged. If considering the opposite subcase, in the condition of a thermally thick slab ($\ell \gg \mu$), the equation 2 reduces to:

$$T_{ac}(r, z = 0) = \frac{P_o}{4\pi K}\int_0^{+\infty} \delta J_o(\delta r)\frac{e^{-(\delta a)^2/8}}{\beta + \frac{h_o}{K}}d\delta \tag{6}$$

This equation has no analytical solution, however, from numerical simulations was concluded that exists a dependence and is $\frac{\delta ln(\sqrt{r} * T_{ac})}{\delta r} = \frac{\delta\phi}{\delta r} = m = \sqrt{\frac{\pi f}{D}} = \mu^{-1}$.

2. Materials

The process of AM is commonly applied to manufacture complex-shaped objects, often with improved performance through topological optimization [69,70]. However,

Table 1.: Printing parameters

PARAMETER	VALUE
Power, P [W]	200
Scan speed V [mm/s]	800
Hatch distance HD [µm]	70
Layer thickness Z [µm]	30

in the present study, simple geometries were used to focus on the correlation between the thermal and electrical properties of AM-processed objects. The case study is an electromagnetic laboratory shield of a relay (Fig. 1). Two sets of tests were performed,

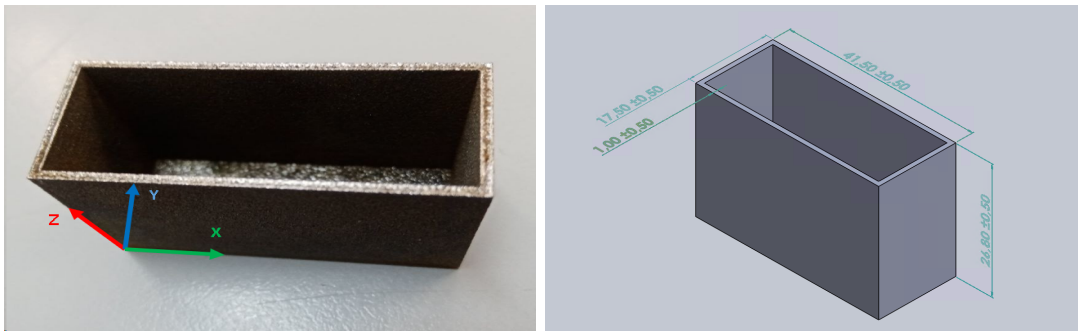

(a) (b)

Figure 1.: Electromagnetic shield FeSi2.9

Alt text: Figure (a): "Photograph of a rectangular, open-top box with a textured surface. The box is oriented such that its length (x-axis) is horizontal and width (y-axis) is vertical in the image plane, with the depth (z-axis) appearing to recede into the page. The x, y, and z axes are indicated by green, blue, and red arrows, respectively." Figure (b): "Three-dimensional CAD rendering of a rectangular box with dimensions labeled. The length is noted as 123.50 mm, width as 48.50 mm, and height as 28.00 mm. The box is shown in perspective view with the dimensions displayed in green text, angled to match the perspective of the box's faces."

the first one on material samples to characterize thermal and electrical conductivity and to validate the Eq.1 for the investigated material and process. The second set was performed on the component to estimate the electrical properties basing on thermal measurements and calibration parameters obtained by the first set. In particular two electromagnetic shields were produced using the Laser Powder Bed Fusion (LPBF) technique from Fe2.9%Si alloy powder [71]. The 3D printer used was a prototype for research purposes and a 200W laser was used to melt the powder in a zig-zag pattern, rotating each layer 67° along the axis of the part being constructed. The construction direction was also along the axis of the produced part. The parameters used in the process are listed in Table 1. Both sets of experiments were performed on AM material as built and heat treated at 1200°C in a vacuum. The heat treatment was optimal to increment magnetic performance [71].

2.1. Powder characterization

Chemical analysis and macro-view of the powders were performed by means of a *SEM EVO-50*, by *Malvern Morpholgy* for the powder morphology study, and *Micrometrics FT4 Powder Rheometer* for the flowability tests. As regards the morphology test, the investigated parameters are $CEDiameter = \sqrt{\frac{4A}{\pi}}[\mu m]$ which is the diameter of a circle with the same projected area A as the particle, and the $Circularity = \sqrt{\frac{4\pi A}{P^2}}$ which quantifies the degree to which the particle is similar to a circle, considering the smoothness of the perimeter P. It quantifies the particle shape and roughness. The flowability test parameters used are constant tip speed (100mm/s), downward anti-clockwise motion (compressive flow mode in the powder), and energy used for tip motion. From the flowability test, the following parameters were obtained: BFE (Basic Flowability Energy) is the energy required to establish a particular flow pattern in a conditioned volume of powder; SE (specific Energy) [mJ/g], a parameter which quantifies how the powder will flow in an unconfined or low stress environment; CBD (Conditioned Bulk Density) [g/ml], that is the density measurement of the powder in the conditioned state; SI (Stability Index), an adimensional ratio to asses if the powder is going to change as a result of being made to flow, FRI (Flow Rate Index), which quantifies the powder sensitivity to flow rate variations.

2.2. Parts characterization

Mass and density differences of printed parts were assessed by measuring the weight of the specimen by an analytical balance (Kern ABJ 220-4NM). To evaluate microstructural differences, which may impact thermal properties, the specimens were prepared for metallographic analysis which was performed by means of optical and electron microscopy techniques. The specimens were cut parallel to the printing plate, hot-mounted in bakelite, and polished to a diamond finish of $1\mu m$ through manual polishing. The sections were then examined using an optical microscope to determine porosity. The samples were chemically etched with 2% Nital to further evaluate microstructural differences, which were then observed using both an optical and scanning electron microscope (SEM). For the SEM analysis, the specimen was studied in a high vacuum and images were acquired using backscattered electrons (BSE) to evaluate the chemical composition of the metal matrix and pores. The porosity percentage was determined over a $28.7mm^2$ area, as shown in Figure 6. The potential presence of inclusions was evaluated through energy-dispersive X-ray spectroscopy (EDS) in points of interest.

3. Methods

3.1. Active Thermography setup

In the thermographic testing, active thermography was considered. It consists in studying the thermal response of a component subjected to an external heat source, in the present case a laser beam, and the corresponding technique is called laser active thermography. The experimental equipment was composed by a thermal camera, a laser excitation source, and a PC control unit. The IR thermal camera is a FLIR A6751sc with a sensitivity lower than 20 mK and 3-5 μm spectral range, while the laser source

Table 2.: FOV info

HFOV	VFOV	IFOV
200mm	160mm	0.32mm

can generate a maximum power of 50 W concentrated in a circular spot of a diameter of 2mm. The experimental configuration was set in reflection mode as shown in Figure 2. To ensure the accuracy of the spatial calibration the thermal camera is positioned perpendicular to the specimen face studied, and the perpendicularity is assured in the vertical and horizontal axis. Two laser stimulation techniques were used. The first technique, called *Pulsed Thermography*, involves the application of an external heat source, in this case, a Gaussian laser beam, for a short period of time to simulate impulsive heating. In the current study, a step pulse was applied. The second technique, called *Lock-In thermography*, involves the application of a repeated step pulse modulated at a specific frequency referred to as the *lock-in frequency*. This technique allows for more advanced signal processing, in phase and frequency, resulting in more consistent and accurate results. The experiments were run at 26.0°C room temperature, relative humidity 30% and a distance between the thermal camera and the target of 530mm. With this setup, the parameters regarding the Field of View are presented in Table 2. To further ensure the accuracy and consistency of the results, special attention was paid to the laser power and frame rate. The laser power was carefully adjusted as indicated to avoid high-temperature increase which could cause non-linearities in the thermal phenomena. Meanwhile, the acquisition frame rate was optimized to obtain the smallest number of frames per test, while still maintaining a high time resolution. The test plan for both specimens was identical and is outlined in Table 3. This consistency in testing methodology allowed for a more accurate comparison of the results between the two specimens. To further validate the results, the data were analyzed by various statistical methods to assess their reliability.

Table 3.: Testing setup

Test	Technique	Step n°/ duration	Power level	Frame rate
1	PULSED	50ms	50%	329fps
2	PULSED	500ms	25%	30fps
3	LOCK-IN	15X50ms	50%	329fps
4	LOCK-IN	15X500ms	25%	30fps
5	LOCK-IN	15x1000ms	15%	60fps

The pulsed tests were processed using the maximum and average temperature information from the thermogram record. In particular, a circular region of interest (ROI) was defined, that is the area where the maximum and average temperatures were obtained. Then, these data were input in a dedicated Matlab routine to study and compare peak temperatures, cooling rate, and logarithmic temperature increase with respect to room temperature. The lock-in test was post-processed to obtain the phase plot of the thermal contours in time. Before extrapolating the phase information, the data were denoised using a singular value decomposition (SVD) denoising algorithm, which reduces the noise in the phase signal for low-amplitude pixels. The phase of the thermal signal was extracted with a dedicated Matlab routine by means of the

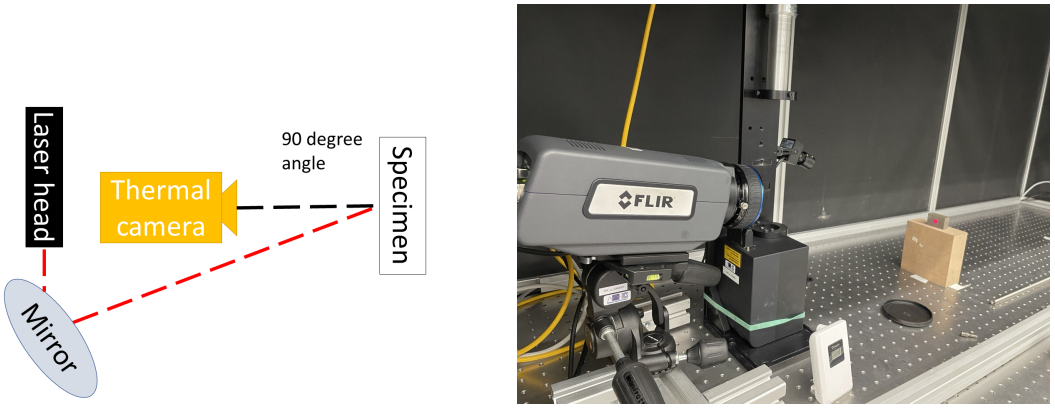

(a) (b)

Figure 2.: Test set-up

Alt text: Figure (a): "Schematic illustration showing the setup of an experiment with a thermal camera setup. A laser head directs a beam towards a mirror, which then redirects the beam at a 90-degree angle towards a specimen. The path of the laser is indicated by a dashed red line. Adjacent to the specimen is a thermal camera, represented by a yellow block, which is positioned to capture the temperature profile of the specimen as the laser interacts with it."
Figure (b): "Photograph of the actual experimental setup. A thermal imaging camera is mounted on a stand, aimed at a specimen located on a table with a dotted pattern. To the left of the camera, a laser apparatus is partially visible. The specimen appears to be a small, square object standing upright on the table. Various other lab equipment and cables are also present around the setup, which is enclosed in a protective area with black walls."

Fast Fourier Transform (FFT), performing a 1D Fourier transform for each pixel. The data are formatted as a tensor of three dimensions, where the first two are the spatial dimensions (pixels) and the third dimension is the time dimension (frames). For each pixel, a Fourier transforms analysis is performed along the time dimension to extrapolate its phase contribution. The result is a 3d phase map plot of the phase value in each pixel in time. In this particular case, the phase map is not intended to detect and display defects, as is commonly done using lamps as heat sources [33,36,72]. Plotting the value of the phase in a given instant along an arbitrary axis passing through the center of the spot, it is expected to be linear according to [68]. The behavior is recognized as symmetric with an almost flat part in the center, which corresponds to the laser spot radius, and a linear part which corresponds to the diffusion area of heat during the lock-in pulsation. The slope of the linear trend is related to thermal diffusivity according to [68]:

$$m = -\sqrt{\frac{\pi f}{D_x}}, \tag{7}$$

where m is the slope [rad/mm] of the linear parte of the phase curve, while f is the modulation frequency [Hz] of the laser spot lock-in stimulation and Dx is the thermal diffusivity [mm2/s] along the X measured surface direction in which phase/space

diagram is plotted by cutting the phase map. The thermal diffusivity is defined as:

$$D_x = \frac{k}{\rho c}. \tag{8}$$

where k is the thermal conductivity $[W/(m*K)]$, ρ is the mass density $[Kg/mm3]$, and c is the specific heat $[J/(Kg*K)]$ The thermal diffusivity along a particular direction can be obtained using the Eq. 7. This methodology allows to obtain thermal diffusivity along any possible direction, avoiding boundary effects, even for small components. Generally speaking, the experimental setup does not permit ideal conditions, that is no noise and an adimensional head source, then, to avoid biases and errors, certain precautions must be taken when selecting the linear zone to evaluate the slope, as follows. The phase plot presents in the center a plateau which corresponds to the area heated by the laser spot. Beyond a certain distance from the laser spot, the data becomes noisy due to the low amplitude of the signal. To minimize these effects, in the present research, all phase data with a phase-amplitude lower than 0.3 K were excluded. In Figure 3a the denoised phase plot for an acquisition on the as built magnetic shield is reported as an example, and in Figure 3b the section of the phase plot according to a generic direction passing through the center of the plot is reported as an example. In Figure 3b, it is evident that there is a typical trend in the phase plot. It can be divided into two separate regions, which are referred to as Zone A and Zone B. Zone A represents the area where the laser beam heats the material and creates a Gaussian-distributed heat flow pulsation, resulting in a plateau on the phase diagram. The size of this plateau is directly related to the radius of the laser beam spot. On the other hand, Zone B represents the regions surrounding the laser spot, where thermal diffusion takes place. The center of circular area of the phase plot, which corresponds to the center of the laser spot, was selected as the origin of a radial coordinate system. This procedure allows for minimizing the impact of any bias or systematic errors in the data. A linear polynomial fitting of the phase-cut in the area surrounding the laser spot is implemented to obtain the slope of the experimental data to calculate the thermal diffusivity m. In order to estimate the slope of the linear part of the phase plot on the same portion of the curve, for different ROIs or for repeated measurements in the same point, a data processing procedure is defined. The linear trend is assumed to start at distance from the origin equal to twice the laser spot radius. The routine flow is the following. A diffusivity parameter D is initialized at a zero value. Then an initial expected thermal diffusivity $D_{expected}$ is defined as equal to an arbitrary value (for example 10). With $D_{expected}$ the corresponding $mu_{expected}$ is calculated according to the formula 9.

$$\mu_{expected} = \sqrt{\frac{D_{expected}}{\pi * f}} \tag{9}$$

This estimated thermal diffusion lenght allows to estimate the initial value of the end extension of the linear trend r_{ext} as :

$$r_{ext} = 2 * r_{laserspot} + 2 * \mu_{expected}. \tag{10}$$

$\mu_{expected}$ permits to uniquely define the area where the initial fit is run, that is in the

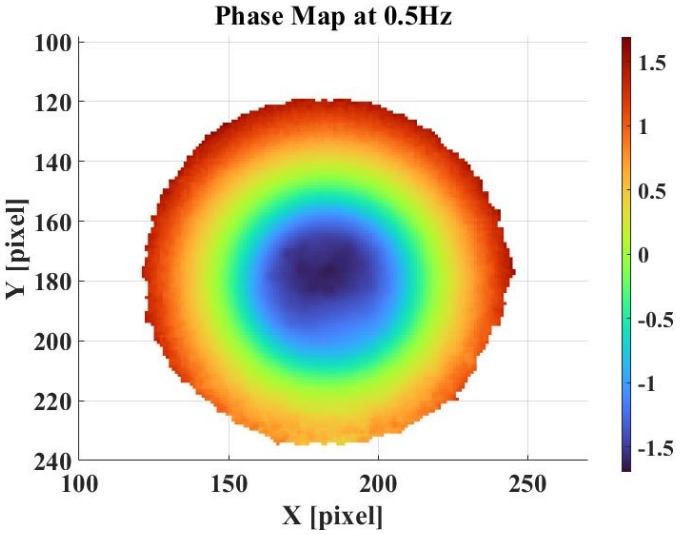

(a) Phase Map example

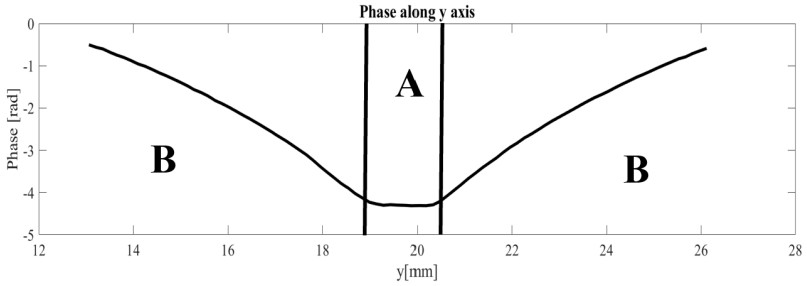

(b) Example of phase plot cut

Figure 3.: Scheme of laser spot and thermal diffusion zone

Alt text: Figure (a): "Color-coded phase map at 0.5 Hz frequency showing a central heat spot with concentric circles of thermal diffusion. The horizontal axis is labeled 'X [pixel]' and ranges from 100 to 250, while the vertical axis is labeled 'Y [pixel]' and ranges from 100 to 240. The colors range from dark blue at the outer edges to red at the center, indicating a gradient in phase values from -1.5 to 1.5 as we move towards the center of the heat spot."

Figure (b): "Graphical representation of a phase plot cut, with the phase angle axis in radians on the vertical axis ranging from -$\pi/2$ to $\pi/2$, and the distance in millimeters on the horizontal axis ranging from 10 to 30 mm. The plot shows a sharp peak in the center labeled 'A' signifying a high phase angle, flanked by two lower regions on either side labeled 'B', indicating a drop in phase angle."

interval within these bounds:

$$[0 + 2 * r_{laserspot}, 0 + 2 * r_{laserspot} + 2 * \mu_{expected}]. \tag{11}$$

Then on the interval between r_{spot} and r_{ext}, the slope of the "linear" curve is calculated and the fitting estimation D_{fit} is obtained. Then the goodness of the fitting is

measured by means of the R^2 of the approximation. If it is acceptable, that is below a given threshold value, then D becomes D_{fit} and the difference between D and $D_{expected}$ compared to a threshold value which depends on the problem and defines the convergence of the problem. According to this last test, the following iteration can improve the estimation or it is stopped. In the scheme Algorithm 1 the algorithm is presented. The modulation frequency is 1Hz (modulation period T= 1s), the diffusivity value are calculated along X and Z directions are presented in fig 1. In figure 4, the fitting made on the linear part of the *phase cut* is reported as an example. It is evident that the trend is strongly linear. For all the fit, the algorithm has given an $R^2 > 0.99$

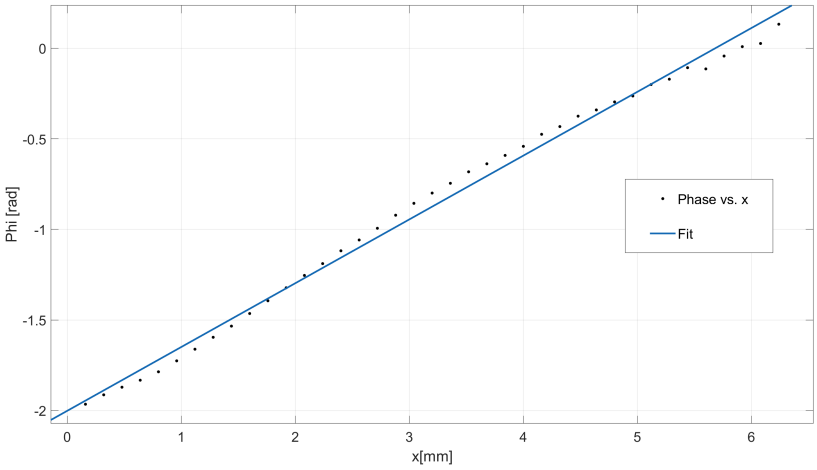

Figure 4.: Fitting line (continuous) and experimental data (dotted)
Alt:text"Scatter plot with fitting line, titled 'Figure 4: Fitting line (continuous) and experimental data (dotted)'. The horizontal axis is labeled 'x [mm]' and ranges from 0 to 6 mm. The vertical axis is labeled 'Phi [rad]' and ranges from -2 to 0 radians. The plot contains a series of black dots representing the experimental data, showing a linear increase in phase with respect to the x-axis. A solid blue line overlays the dots, representing the linear fit to the data. The legend in the top right corner identifies the black dots as 'Phase vs. x' and the blue line as 'Fit'."

3.1.1. On the thermal diffusion length

The driving parameter in choosing the correct lock-in frequency, in addition to the thermal camera sampling frequency and noise-to-signal ratio, is the thermal diffusion length. In fact, from this value derives a change from thermally thin to thermally thick behavior. As presented in Equation9 the expected thermal diffusion length depends on expected thermal diffusivity and lock-in frequency. In the case of an anisotropic material, this value can give an indication of how affordable the measurement is. In this case, in order to avoid any influence of sub-superficial defects, the best way to conduct the measurement is to avoid using a lock-in frequency which gives a thermal diffusion length smaller than the specimen's thickness.

Algorithm 1 Calculate Thermal Diffusivity

Find the center of the laser spot in the phase diagram
Cut_x and Cut_y as the phase plots in directions parallel respectively to the x and y axis and passing through the center.
Define an expected thermal diffusivity D_{exp}, the radius of the laser spot r, and the modulation frequency of the laser f

Require: $D_{exp} \geq 0$ and $r_{spot} \geq 0$ and $f \geq 0$

$\mu_{exp} = \sqrt{\frac{D_{exp}}{\pi f}}$
$r_{start} = 2 * r_{spot}$
$r_{end} = r_{start} + 2 * \mu_{exp}$
D=0
while $|D - D_{expected}| > 2mm^2/s$ **do**
    execute matlab fitting algorithm along Cut_x and Cut_y to calculate D_{fit}
    if $R^2 > 0.99$ **then**
        $D = D_{fit}$
    end if
    if $|D - D_{expected}| < 2mm^2/s$ **then**
        Diffusivity measurement is reliable
    else
        Change D_{exp} with D
    end if
end while

3.2. Electrical conductivity measurement

According to [73], electrical conductivity was measured on dedicated specimens by means of a four-wire test using a system consisting of the following two PC-controlled instruments: Fluke 5720A multi-function calibrator, working as a direct current generator, and Keythley 2002 digital multimeter, used as a direct voltage meter. The controlling software operates repeated polarity changes on the current, in order to allow the elimination of offsets due to the multimeter.

Specimen electrical conductivity value was therefore measured by measuring the resistivity of a bar of Fe-2.9wt%Si with the four-point probes technique. This procedure is widely described in [74]. The measuring circuit is shown in Fig.5. The current passes through the outer probes and the voltage is measured through the inner probes. Using Ohm's second law (Eq.12), it is possible, knowing the geometry of the piece, to derive the resistivity of the material and then the electrical conductivity:

$$R = \rho \cdot \frac{l}{S} \tag{12}$$

The tests were carried out on 10 cylindrical specimens, 5 as built and 5 heat treated. On each specimen, 3 repetitions were performed. The electrical conductivity was measured parallel to the axis of the specimen.

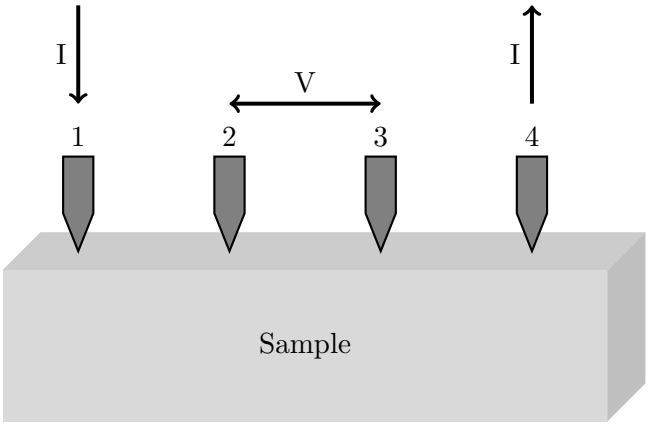

Figure 5.: 4-point probe test setup. Current is applied through probes 1 and 4, while voltage is measured across probes 2 and 3.

Alt text:"Diagram of a 4-point probe test setup on a rectangular sample block. Four numbered probes, represented by arrowheads, are arranged in a line on top of the sample. Arrows labeled with the letter 'I' point downwards onto probes 1 and 4, indicating the direction of current application. Between probes 2 and 3, a double-sided horizontal arrow labeled 'V' denotes the measurement of voltage. The diagram illustrates that current is applied through probes 1 and 4, while the voltage is measured across probes 2 and 3, as stated in the caption 'Figure 5: 4-point probe test setup. Current is applied through probes 1 and 4, while voltage is measured across probes 2 and 3.'"

4. Results

4.1. Powder characterization

In Table 4 the morfological characterization results are reported.

Table 4.: Powder Morphology results

PARAMETER	VALUE
CE Diameter Minimum [μ m]	2.02
CE Diameter Maximum [μ m]	241.75
Particles counted [-]	33845
CE Diameter D[v,0.1]	30.33
CE Diameter D[v,0.5]	71.32
CE Diameter D[v,0.9]	166.9
CE Diameter STDV [μ m]	17.83
Circularity Minimum [-]	0.000
Circularity Maximum [-]	1.000
Circularity Mean [-]	0.934
Circularity D[n,0.1]	0.867
Circularity D[n,0.5]	0.940
Circularity D[n,0.9]	0.991
Circularity STDV [μ m]	0.057

The powder flowablity test results are presented in table 5. The value of SE, which

Table 5.: Powder Flowability results

PARAMETER	VALUE
BFE[mJ]	409(± 1.68%)
SE[mJ/Kg]	2.25(±0.720%)
CBD[g/ml]	3.27(±0.298%)
SI[-]	0.986(±1.47%)
FRI[-]	1.11(±0.207%)
Initial mass[g]	92.1(± 0.0135%)

is lower than 5, means that the powder does not show cohesion tendency; SI ≈ 1 means that the powder is robust, and not affected by flow effects; FRI ≈ 1 that means that the powder behaviour is not dependent on the flow rate, as typical for the high scatter of granulometry. SEM analysis confirmed that the powder grains have an highly irregular and rough shape and a scattered granulometry .

4.2. Parts characterization

The two shields, as built and heat treated, were polished on the X-Y deposition plane, then the optical microscopy images were acquired in order to evaluate presence, geometry and percentage of pores. The comparison of two different images highlighting the presence of pores is presented in 6. In Table 6 the corresponding results of image processing for porosity estimation are reported. The same specimens were chemically etched in order to point out microstructural differences. In Figure 8 is presented an overview of the two metallurgical structures, while in A1 is presented as a microstructural comparison at high magnification. It results that heat treatment reduces the porosities and modifies the microstructure, as already evident in the literature. The BSE analysis assesses the presence of porosities or eventual precipitates. In figure A2c the BSE map points out the precipitates in as-built specimens as red points. The chemical composition of the two specimens is similar, the porosities have a composition similar to the rest of the material. In order to investigate the chemical composition on a specific point a local EDS measurement was performed. Figure A4 shows the EDS weight percentage value obtained at the red point in Figure A2c, which may be attributed to a FeSi precipitate with a weight percentage of 66.5% Fe and 33.5% Si.

Table 6.: Pores percentage

	AsBuilt	HeatTreated
Pore Percentage	4.667%	0.178%

4.3. Thermographic analysis

This analysis is focused on two directions. In the first one the effects of thermal treatment of thermal properties are reported and discussed. In the second, the relation between thermal and electrical measurements are reported and discussed. The pulsed technique did not give any evident indication since the influence of photo-thermal properties of the studied surface affect the results more than the microstructural differences

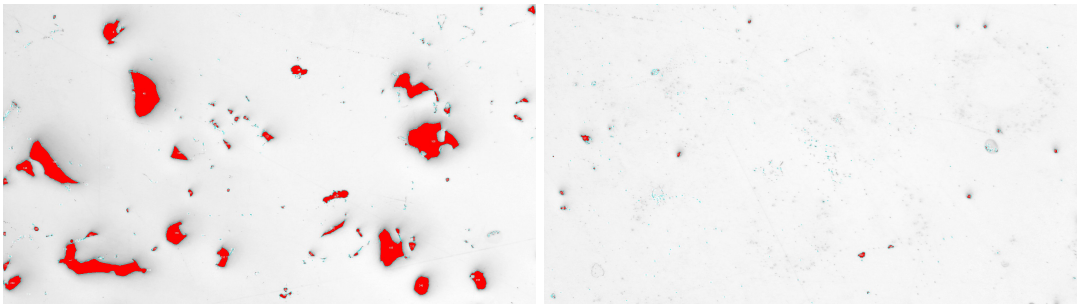

(a) As-Built (b) Heat-Treated

Figure 6.: Porosities on sample surface

Alt text:"(a) As-Built: A microscopic image of a sample surface showing various sized porosities. The majority of the background is white, indicating the solid material, while the porosities are clearly visible as irregularly shaped red areas scattered across the surface, with some small spots appearing in a deep blue color." "(b) Heat-Treated: A similar microscopic image of a sample surface after heat treatment. The background remains predominantly white. There are significantly fewer and smaller red areas, indicating porosities, and the blue spots are also reduced, suggesting a denser and more uniform structure compared to the as-built state."

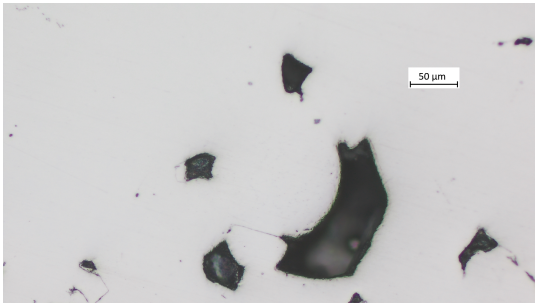

Figure 7.: Detail of a porosity

Alt text:"A microscopic image showing a close-up view of a porosity in a material. The porosity appears as a large, irregularly shaped dark area with jagged edges on a white background, indicating the surrounding solid matrix. A scale bar in the corner provides a measurement reference, indicating that the width of the field is 50 micrometers."

in the partes. Then in the following the results of Lock-in analysis are presented. The first analysis is based on the evidence that variations in material thermal properties, due to structural modifications, can be measured as a phase delay in thermal diffusion through the material bulk. The goal of this analysis is to quantify the effect of heat treatment on the additively manufactured shields thermal diffusivity. The hypothesis is that the heat treatment decreases the number of voids in the specimen and, as a consequence, it increases its thermal diffusivity. This increment in thermal diffusivity can be observed as a modified phase delay (slope) around the phase plot corresponding to the laser spot. This is supported by the analytical study performed by Mendioroz in [68], where it was shown that a lower thermal diffusivity corresponds to a steeper slope on the phase diagram. The lock-in tests were conducted on the largest face of

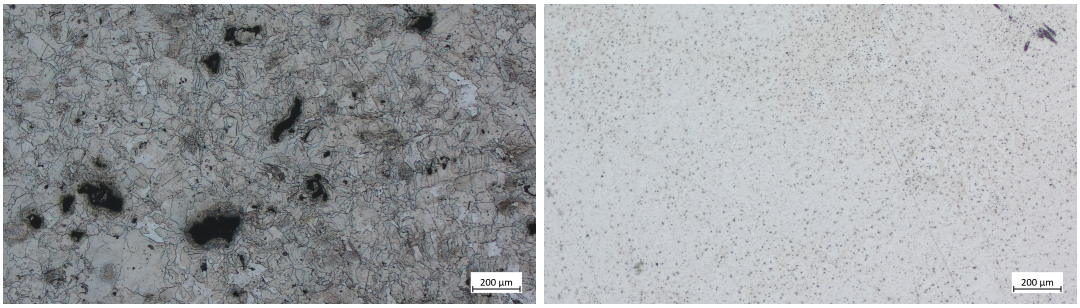

(a) As-Built (b) Heat-Treated

Figure 8.: Sample microstructure

Alt text:"(a) As-Built: A microscopic image of a material's microstructure, showing a network of dark, irregularly shaped porosities distributed within a gray matrix with a web-like pattern, suggesting a granular structure. A scale bar indicates a 200-micrometer field width. (b) Heat-Treated: A similar microscopic image where the material exhibits a significantly more homogeneous and refined structure with a reduction in visible porosities and a lighter, more uniform gray color overall. The scale bar also denotes a 200-micrometer field width."

the magnetic shield, parallel to the X-Z axis of the printer. The thermal diffusivity was measured along X and Z directions. It is important to note that the electrical measurements were performed along the Z difrection, coresponding to cylinder axis and deposition direction. Hence, the empirical model of Eq(1) will be calibrated using the thermal diffusivity measurements along the Z-axis. By presenting these results in both the X and Z axis, a comprehensive understanding of the thermal behavior of the magnetic shielding can be gained. The results of the annealing treatment on the specimen can be observed in Figure 9, which displays a detail of the phase diagram. As shown in the figure, there is a noticeable difference in slope between the as-built and annealed specimens. In fact, after the annealing treatment, the slope of the curve for the annealed specimen is less steep, indicating that the thermal diffusivity of the material has increased. This finding supports the conclusion that annealing treatments can improve the thermal properties of materials, resulting in increased thermal diffusivity. All the results obtained from the thermal measurement in the 2 magnetic shielding are presented in Tab. 7: For the thin surface of the magnetic shielding (X-Z

Table 7.: Experimental diffusivity results for the shield samples and 4pp specimen

	$D_x[mm^2/s]$	R_x^2	$D_z[mm^2/s]$	R_z^2	$D_{avg}[mm^2/s]$
As-Built	7.14	0.9985	6.90	0.9979	7.018
Heat Treated	8.054	0.9970	7.65	0.9964	7.853
4PP specimen	5.23	0.9968	6.80	0.9984	6.02

plane) the thermal diffusivity differs in the X and Z directions. In both cases, heat treated and as built, the wall diffusivity is larger along X direction than along Z axis. This could be related to the fact that the weld pools worsen the thermal diffusivity. Furthermore, the heat treatment improves the thermal properties of the material, as it happened for the electric properties. This may be linked to the microstructural results. Surely the improvement of material density, due to the heat treatment, increases the thermal conductivity, in literature this phenomenon is well known [75]. In

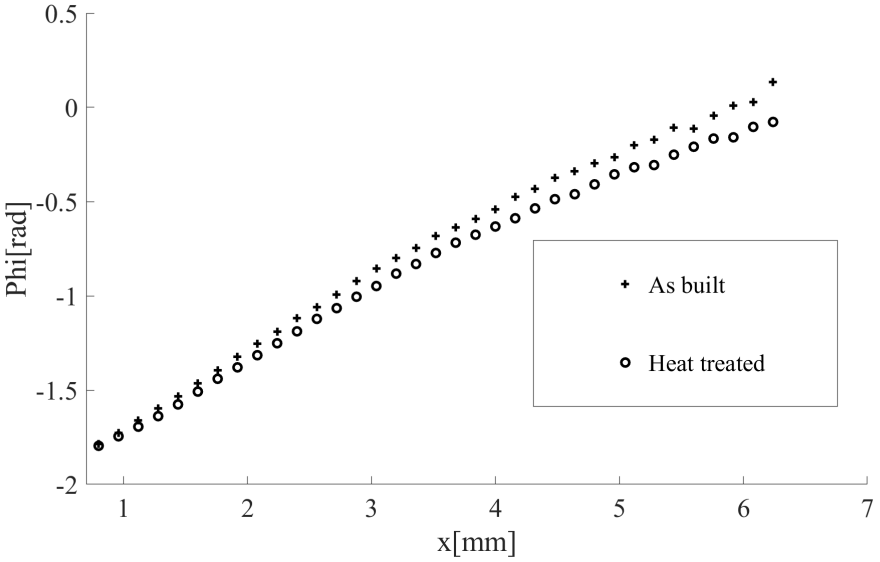

Figure 9.: Experimental phase value out of the laser spot interval
Alt text:"Scatter plot comparing the phase values of two different material conditions: 'As built', shown as black plus signs, and 'Heat treated', shown as hollow circles, over a distance measured in millimeters. Both datasets display a negative slope, with phase values decreasing as distance increases. The 'As built' data begins at just below -1.5 radians and trends upwards to around -0.5 radians at 7 mm, while the 'Heat treated' data starts at -2 radians, trending upwards more gently and remaining lower than the 'As built' data throughout the distance range."

addition, different microstructures, with different composition and grain size, tends to show different thermal properties. The change in properties due to heat treatment is quantified by evaluating the ratio of each parameter (thermal diffusivity along X and Z axes and electric conductivity) between as built and heat treated, multiplied by 100, as reported in Table 8. It can be observed that in all cases the heat-treated material shows improved electrical conductivity and thermal diffusivity properties. The percent difference between these two properties is similar. For what concerns thermal conductivity further consideration will follow in the next section. For what

Table 8.: AsBuilt/HeatTreated thermal and electrical coefficents ratio

	D_x	D_z	D_{avg}	σ_{exp}	pore percentage
AB/HT [%]	88.6	90.2	89.37	83.02	95.5

concerns the second experimental line, an active thermography test was performed on the heat-treated specimen used for the four-point probe (4PP) test, to calibrate the Eq(1) model used to predict the electrical conductivity from thermal parameters. The results of the active thermography tests performed on the 4PP annealed specimen are presented in Table 7. It results that the highest value of diffusivity for heat-treated specimens is along Z direction D_z. In particular, the results of the experimental measurement of electrical conductivity in the 4PP heat treated specimen are presented in Table 9 where the mean value of the measurements are reported. The variations of

the different measurements ranges always within the 5% of the presented mean values. These results will be discussed in the next section

4.4. Properties correlation and further comments

Once obtained the thermal conductivity for as built and heat treated shields by means of the phase slope method, this parameter can be used to calibrate the Weidemann-Franz law, and to predict the electrical conductivity of the magnetic shield in the two material configuration. By means of experimental results on thermal diffusivity

Table 9.: Electrical conductivity of the specimen

	As-built	Annealed
σ [S/m]	1.76 E06	2.12 E06

and on electrical conductivity for heat treated 4PP specimens, the Lorentz constant is obtained. It is known from literature that experimental values can be significantly different from theoretical ones [75,76]. Then the Lorentz constant needs to be adjusted so that $\sigma_{predicted} = \sigma_{experimental}$. Some assumptions need to be made in order to perform this calculation, including the specific heat being assumed to be $444\frac{J}{KgK}$, which is the reference value for pure Fe, and the density being assumed to be $7800\frac{Kg}{m^3}$. The resulting Lorentz constant is L=3.23E-08, which will be used to predict the electrical conductivity of the shield components. Once the constant is estimated on the material then a prediction of electric conductivity can be obtained for the component operating the adequate corrections, for example using the same specific heat ($444\frac{J}{KgK}$), but the density of $7800\frac{Kg}{m^3}$ being scaled based on the porosity level. The resulting predictions are presented in Table 10. The results of the heat treatment on the shield shown a

Table 10.: Electric conductivity prediction

	σ_x [E06]	σ_z[E06]	$\sigma_{avg}[E06]$
As built	2.17	2.10	2.13
Heat treated	2.52	2.39	2.45

positive impact on its thermal diffusivity. The heat treatment at high temperatures causes a decrease in porosity, leading to an increase in both thermal and electrical conductivity. The increment of electric conductivity is generated by the same phenomenon which increments the thermal diffusivity and conductivity. The Wiedemann - Franz relation (Eq.(1)) is validated by the present results thus allowing to state that it is possible to estimate local and directional electric conductivity in AM parts by means of AT Lock In non destructive analysis.

5. Conclusion

In this work, a method is proposed and validated for non destructive estimation of electric conductivity in additive manufactured components by means of active thermography technique. This procedure well applies when obtaining complex shapes by

means of AM affects material properties due to process. The procedure of active thermography resulted to be useful for the evaluation not only of the thermal parameters but also the electrical ones thanks to an empirical relationship linking these properties. Thanks to this procedure, manufacturing of dedicated specimens for electric properties characterization is not required: the estimation of electric properties can be directly performed on the finished part even if it has a complex shape, by means of non-destructive IR thermographic measurements. The results show a negligible difference between the experimental electric conductivity and the estimated one. The experimental measurements were performed using active thermography and a 4-point probe test. The results showed that the annealed specimen had better thermal diffusivity than the as-built one. This improvement can be attributed to the decrease in voids and pores caused by the heat treatment, leading to higher thermal conductivity and, as a consequence, higher electrical conductivity. To predict the electrical conductivity, the Wiedemann-Franz law was applied using the thermal diffusivity obtained from the phase method. The Lorentz constant was adjusted to match the experimental value of electrical conductivity. The results showed that the predicted electrical conductivity matched well with the experimental measurements. The same methodology was applied to calculate the predicted electrical conductivity of the magnetic shielding. In conclusion, the use of both Pulsed Thermography and Lock-thermography techniques allowed obtaining accurate and reliable prediction of electric conductivity in AM parts. The consistent test plan applied to both specimens further ensured the validity of the findings, and the use of statistical analysis provided additional confidence in the results. In conclusion, the results provide valuable insights into the thermal properties of magnetic shielding. The information obtained from these tests will be instrumental in further refining and improving the model used to predict the thermal behavior of the magnetic shielding. Furthermore, the results showed that the heat treatment of the specimen leads to an increase in thermal diffusivity and, as a consequence, in electrical conductivity. In conclusion, this study provides a contribution to the understanding of the thermal and electrical behavior of AM magnetic components.

Acknowledgement

Acknowledgement is given to the research group of Professor Barbara Previtali of the Politecnico di Milano for the realisation of the components produced by Additive Manufacturing technology

References

[1] Tofail SA, Koumoulos EP, Bandyopadhyay A, et al. Additive manufacturing: scientific and technological challenges, market uptake and opportunities. Materials Today. 2018;21(1):22–37. Available from: https://www.sciencedirect.com/science/article/pii/S1369702117301773.

[2] Wang H, Feng W, Liu D, et al. Iron-based soft magnetic materials fabricated by laser additive manufacturing. Engineered Science. 2023;22:809.

[3] Galarreta-Rodriguez I, Lopez-Ortega A, Garayo E, et al. Magnetically activated 3d printable polylactic acid/polycaprolactone/magnetite composites for magnetic induction heating generation. Advanced Composites and Hybrid Materials. 2023;6(3):102.

[4] Jambhulkar S, Ravichandran D, Thippanna V, et al. A multimaterial 3d printing-assisted

micropatterning for heat dissipation applications. Advanced Composites and Hybrid Materials. 2023;6(3):1–16.
[5] Wang X, Liu Z, Wang H, et al. Direct 3d printing of piezoelectrets: process feasibility, prototypes fabrication and device performance. Engineered Science. 2022;21:800.
[6] Manoj A, Ch R, et al. Biodegradable filament for 3d printing process: A review. Engineered Science. 2022;18:11–19.
[7] Wang X, Liu Z, Wang H, et al. An electro-mechanical coupled model for 3d printed piezoelectrets: Development, validation, and prediction. Engineered Science. 2023;24:899.
[8] Zhang X, Dong M, Cai X, et al. Progress in machining-induced residual stress and microstructural evolution of inhomogeneous materials and composites. Advanced Composites and Hybrid Materials. 2023;6(3):122.
[9] Uriondo A, Esperon-Miguez M, Perinpanayagam S. The present and future of additive manufacturing in the aerospace sector: A review of important aspects. Proceedings of the Institution of Mechanical Engineers, Part G: Journal of Aerospace Engineering. 2015; 229(11):2132–2147. Available from: https://doi.org/10.1177/0954410014568797.
[10] Beyer C. Strategic Implications of Current Trends in Additive Manufacturing. Journal of Manufacturing Science and Engineering. 2014 10;136(6). 064701; Available from: https://doi.org/10.1115/1.4028599.
[11] Rauch E, Unterhofer M, Dallasega P. Industry sector analysis for the application of additive manufacturing in smart and distributed manufacturing systems. Manufacturing Letters. 2018;15:126–131. Industry 4.0 and Smart Manufacturing; Available from: https://www.sciencedirect.com/science/article/pii/S2213846317300925.
[12] Subramaniyan AK, Reddy AS, Mathias S, et al. Influence of post-processing techniques on the microstructure, properties and surface integrity of al si mg alloy processed by laser powder bed fusion technique. Surface coatings technology. 2021;425:127679.
[13] Raja A, Cheethirala SR, Gupta P, et al. A review on the fatigue behaviour of alsi10mg alloy fabricated using laser powder bed fusion technique. Journal of materials research and technology. 2022;17:1013–1029.
[14] Garibaldi M, Ashcroft I, Hillier N, et al. Relationship between laser energy input, microstructures and magnetic properties of selective laser melted fe-6.9%wt si soft magnets. Materials characterization. 2018;143:144–151.
[15] Choo H, Sham KL, Bohling J, et al. Effect of laser power on defect, texture, and microstructure of a laser powder bed fusion processed 316l stainless steel. Materials design. 2019;164:107534.
[16] Brennan MC, Keist JS, Palmer TA. Defects in Metal Additive Manufacturing Processes. Journal of Materials Engineering and Performance. 2021 Jul;30(7):4808–4818. Available from: https://doi.org/10.1007/s11665-021-05919-6.
[17] Charalampous P, Kostavelis I, Tzovaras D. Non-destructive quality control methods in additive manufacturing: a survey. Rapid Prototyping Journal. 2020 Jan;26(4):777–790. Publisher: Emerald Publishing Limited; Available from: https://doi.org/10.1108/RPJ-08-2019-0224.
[18] Everton SK, Hirsch M, Stravroulakis P, et al. Review of in-situ process monitoring and in-situ metrology for metal additive manufacturing. Materials Design. 2016;95:431–445. Available from: https://www.sciencedirect.com/science/article/pii/S0264127516300995.
[19] Zhang B, Liu S, Shin YC. In-process monitoring of porosity during laser additive manufacturing process. Additive Manufacturing. 2019;28:497–505. Available from: https://www.sciencedirect.com/science/article/pii/S2214860419303653.
[20] Tapia G, Elwany A. A Review on Process Monitoring and Control in Metal-Based Additive Manufacturing. Journal of Manufacturing Science and Engineering. 2014 10;136(6). 060801; Available from: https://doi.org/10.1115/1.4028540.
[21] Carvalho MS, Martins AP, Santos TG. Simulation and validation of thermography inspection for components produced by additive manufacturing. Applied Thermal Engineering. 2019;159:113872. Available from: https://www.sciencedirect.com/science/article/pii/S1359431119308506.

[22] Senck S, Happl M, Reiter M, et al. Additive manufacturing and non-destructive testing of topology-optimised aluminium components. Nondestructive Testing and Evaluation. 2020 Jul;35(3):315–327. Publisher: Taylor & Francis _eprint: https://doi.org/10.1080/10589759.2020.1774582; Available from: https://doi.org/10.1080/10589759.2020.1774582.

[23] Lu QY, Wong CH. Applications of non-destructive testing techniques for post-process control of additively manufactured parts. Virtual and Physical Prototyping. 2017 Oct;12(4):301–321. Publisher: Taylor & Francis _eprint: https://doi.org/10.1080/17452759.2017.1357319; Available from: https://doi.org/10.1080/17452759.2017.1357319.

[24] Kolb CG, Zier K, Grager JC, et al. An investigation on the suitability of modern nondestructive testing methods for the inspection of specimens manufactured by laser powder bed fusion. SN Applied Sciences. 2021 Jun;3(7):713. Available from: https://doi.org/10.1007/s42452-021-04685-3.

[25] Silbernagel C, Ashcroft I, Dickens P, et al. Electrical resistivity of additively manufactured alsi10mg for use in electric motors. Additive Manufacturing. 2018;21:395–403. Available from: https://www.sciencedirect.com/science/article/pii/S2214860418300769.

[26] Garibaldi M, Ashcroft I, Lemke J, et al. Effect of annealing on the microstructure and magnetic properties of soft magnetic fe-si produced via laser additive manufacturing. Scripta Materialia. 2018;142:121–125. Available from: https://www.sciencedirect.com/science/article/pii/S1359646217305067.

[27] Wang C, Liu X, Yang T, et al. An overview of metal-organic frameworks and their magnetic composites for the removal of pollutants. Separation and Purification Technology. 2023;:124144.

[28] Zeng J, Xie W, Guo Y, et al. Magnetic field facilitated electrocatalytic degradation of tetracycline in wastewater by magnetic porous carbonized phthalonitrile resin. Applied Catalysis B: Environmental. 2024;340:123225.

[29] Cheng H, Xing L, Zuo Y, et al. Constructing nickel chain/mxene networks in melamine foam towards phase change materials for thermal energy management and absorption-dominated electromagnetic interference shielding. Advanced Composites and Hybrid Materials. 2022;5(2):755–765.

[30] Xie W, Yao F, Gu H, et al. Magnetoresistive and piezoresistive polyaniline nanoarrays in-situ polymerized surrounding magnetic graphene aerogel. Advanced Composites and Hybrid Materials. 2022;5(2):1003–1016.

[31] Gao T, Rong H, Mahmoud KH, et al. Iron/silicon carbide composites with tunable high-frequency magnetic and dielectric properties for potential electromagnetic wave absorption. Advanced Composites and Hybrid Materials. 2022;5(2):1158–1167.

[32] Kan A, Zhang Q, Cao D. Innovation on thermal conductivity measurement device of vacuum insulation panel with double hemispheres chambers. ES Energy & Environment. 2021;15:28–33.

[33] Doshvarpassand S, Wu C, Wang X. An overview of corrosion defect characterization using active infrared thermography ; 2019.

[34] Thiel E, Kreutzbruck M, Ziegler M. Laser Projected Photothermal Thermography for Characterizing Hidden Defects; 2016.

[35] Salazar A, Mendioroz A, Oleaga A. Flying spot thermography: Quantitative assessment of thermal diffusivity and crack width. Journal of Applied Physics. 2020 4;127.

[36] Maierhofer C, Myrach P, Krankenhagen R, et al. Detection and characterization of defects in isotropic and anisotropic structures using lockin thermography. Journal of Imaging. 2015 dec;1(1):220–248.

[37] Guo X, Vavilov V. Crack detection in aluminum parts by using ultrasound-excited infrared thermography. Infrared Physics and Technology. 2013;61:149–156.

[38] Park H, Choi M, Park J, et al. A study on detection of micro-cracks in the dissimilar metal weld through ultrasound infrared thermography. Infrared Physics and Technology. 2014 jan;62:124–131.

[39] Yi Q, Malekmohammadi H, Tian GY, et al. Quantitative Evaluation of Crack Depths on Thin Aluminum Plate Using Eddy Current Pulse-Compression Thermography. IEEE Transactions on Industrial Informatics. 2020 jun;16(6):3963–3973.
[40] Yuan B, Spiessberger C, Waag TI. Eddy current thermography imaging for condition-based maintenance of overlay welded components under multi-degradation. Marine Structures. 2017 may;53:136–147.
[41] Goldammer M, Mooshofer H, Rothenfusser M, et al. Automated induction thermography of generator components. In: AIP Conference Proceedings; Vol. 1211; 2010. p. 451–457.
[42] Dell'Avvocato G, Palumbo D, Galietti U. A non-destructive thermographic procedure for the evaluation of heat treatment in Usibor®1500 through the thermal diffusivity measurement. NDT and E International. 2023 jan;133.
[43] Sesana R, Santoro L, Curà F, et al. Assessing thermal properties of multipass weld beads using active thermography: microstructural variations and anisotropy analysis. International Journal of Advanced Manufacturing Technology. 2023;.
[44] Kato H, Baba T, Okaji M. Anisotropic thermal-diffusivity measurements by a new laser-spot-heating technique. Measurement Science and Technology. 2001;12:2074–2080.
[45] Wolf A, Pohl P, Brendel R. Thermophysical analysis of thin films by lock-in thermography. Journal of Applied Physics. 2004;96(11):6306–6312. Available from: https://doi.org/10.1063/1.1811390.
[46] Ishizaki T, Nagano H. Measurement of Three-Dimensional Anisotropic Thermal Diffusivities for Carbon Fiber-Reinforced Plastics Using Lock-In Thermography. International Journal of Thermophysics. 2015;36(10-11):2577–2589.
[47] Strzałkowski K, Streza M, Dadarlat D, et al. Thermal characterization of II-VI binary crystals by photopyroelectric calorimetry and infrared lock-in thermography. Journal of Thermal Analysis and Calorimetry. 2015;119(1):319–327.
[48] Philipp A, Pech-May NW, Kopera BA, et al. Direct measurement of the in-plane thermal diffusivity of semitransparent thin films by lock-in thermography: An extension of the slopes method. Analytical Chemistry. 2019;91(13):8476–8483. Available from: www.goodfellow.com;.
[49] Bavastro D, Canova A, Giaccone L, et al. Numerical and experimental development of multilayer magnetic shields. Electric Power Systems Research. 2014;116:374–380. Available from: https://www.sciencedirect.com/science/article/pii/S0378779614002375.
[50] International Commission on Non-Ionizing Radiation Protection (ICNIRP). Guidelines for limiting exposure to time-varying electric and magnetic fields (1 Hz to 100 kHz). Health Physics. 2010 Dec;99(6):818–836.
[51] Salinas E, Bottauscio O, Chiampi M, et al. Mitigation techniques of power frequency magnetic fields originated from electric power systems; 2009.
[52] Quercio M, Galbusera F, Canova A, et al. Electromagnetic shielding properties of lpbf produced fe2. 9wt.% si alloy. Journal of Physics: Energy. 2023;5(4):045003.
[53] Canova A, Corti F, Laudani A, et al. Innovative shielding technique for wireless power transfer systems. IET Power Electronics. 2023;.
[54] Quercio M, Barlassina L, Canova A. Characterization of the shielding properties of a power transformer enclosure. In: IEEE EUROCON 2023-20th International Conference on Smart Technologies; IEEE; 2023. p. 349–353.
[55] Quercio M, Campanelli F, Canova A. Passive loop optimisation for hv joint zone. In: IEEE EUROCON 2023-20th International Conference on Smart Technologies; IEEE; 2023. p. 343–348.
[56] Canova A, Quercio M. A shielding system proposal for the cabling of electric glass melters. IEEE Open Journal of Industry Applications. 2023;4:1–10.
[57] Yu J, Zhang Y, Guo Q, et al. Effect of pressure on anisotropy in elasticity, sound velocity, and thermal conductivity of vanadium borides. Advanced Composites and Hybrid Materials. 2022;5(3):2297–2305.
[58] Wei D, Weng M, Mahmoud M, et al. Development of novel biomass hybrid aerogel supported composite phase change materials with improved light-thermal conversion and

thermal energy storage capacity. Advanced Composites and Hybrid Materials. 2022; 5(3):1910–1921.
[59] Jing X, Li Y, Zhu J, et al. Improving thermal conductivity of polyethylene/polypropylene by styrene-ethylene-propylene-styrene wrapping hexagonal boron nitride at the phase interface. Advanced Composites and Hybrid Materials. 2022;5(2):1090–1099.
[60] Lu LX, Wang XL, Li SL, et al. Thermal performance of lonicera rupicola grass as a building insulation composite material. Advanced Composites and Hybrid Materials. 2023; 6(1):8.
[61] Chang Z, Yuan K, Li J, et al. Anomalous thermal conductivity induced by high dispersive optical phonons in rubidium and cesium halides. ES Energy & Environment. 2022;16:30–39.
[62] Review on engineering designing of electromagnetic interference shielding materials using additive manufacturing. Polymer Composites. 2022;43(7):4081–4099. Available from: https://onlinelibrary.wiley.com/doi/abs/10.1002/pc.26684.
[63] Abedi K, Miri S, Gregorash L, et al. Evaluation of electromagnetic shielding properties of high-performance continuous carbon fiber composites fabricated by robotic 3d printing. Additive Manufacturing. 2022;54:102733. Available from: https://www.sciencedirect.com/science/article/pii/S2214860422001373.
[64] Lee KPM, Baum T, Shanks R, et al. Electromagnetic interference shielding of 3d-printed graphene–polyamide-6 composites with 3d-printed morphology. Additive Manufacturing. 2021;43:102020. Available from: https://www.sciencedirect.com/science/article/pii/S2214860421001858.
[65] Tritt TM. Thermal Conductivity: Theory, Properties, and Applications (Physics of Solids and Liquids). ; 2004.
[66] Graf MJ, Yip S, Sauls JA, et al. Electronic thermal conductivity and the wiedemann-franz law for unconventional superconductors. Physical Review B. 1996;53(22):15147.
[67] Völklein F, Reith H, Cornelius T, et al. The experimental investigation of thermal conductivity and the wiedemann–franz law for single metallic nanowires. Nanotechnology. 2009;20(32):325706.
[68] Mendioroz A, Fuente-Dacal R, Apianiz E, et al. Thermal diffusivity measurements of thin plates and filaments using lock-in thermography. Review of Scientific Instruments. 2009; 80.
[69] Canova A, Gruosso G, Quercio M. Characterization of Electromagnetic Device by Means of Spice Models. International Journal of Emerging Technology and Advanced Engineering. 2021 Sep;11(9):12–22. Available from: https://ijetae.com/files/Volume11Issue9/IJETAE$_0$921$_0$2.*pdf*.
[70] Jihong Z, Han Z, Chuang W, et al. A review of topology optimization for additive manufacturing: Status and challenges. Chinese Journal of Aeronautics. 2021;34(1):91–110.
[71] Quercio M, Galbusera F, Pošković E, et al. Functional characterization of l-pbf produced fesi2.9 soft magnetic material. In: 2022 International Conference on Electrical Machines (ICEM); 2022. p. 531–537.
[72] Bari P, Japigia V. Data processing procedures for defects evaluation in composite materials by means of stimulated thermography. In: 19th World Conference on Non-Destructive Testing 2016; 2016. p. 1–9. Available from: http://creativecommons.org/licenses/by/3.0/.
[73] Waremra RS, Betaubun P. Analysis of Electrical Properties Using the four point Probe Method. 2018 Aug;73:13019. Conference Name: E3S Web of Conferences ADS Bibcode: 2018E3SWC..7313019W; Available from: https://ui.adsabs.harvard.edu/abs/2018E3SWC..7313019W.
[74] Lüpke F, Cuma D, Korte S, et al. Four-point probe measurements using current probes with voltage feedback to measure electric potentials. Journal of Physics: Condensed Matter. 2018 Jan;30(5):054004. Publisher: IOP Publishing; Available from: https://dx.doi.org/10.1088/1361-648X/aaa31e.
[75] Raab SJ, Guschlbauer R, Lodes MA, et al. Thermal and Electrical Conductivity of 99.9% Pure Copper Processed via Selective Electron Beam Melt-

ing. Advanced Engineering Materials. 2016;18(9):1661–1666. Available from: https://onlinelibrary.wiley.com/doi/10.1002/adem.201600078.
[76] Hatakeyama T, Kibushi R, Ishizuka M, et al. Fundamental study of surface roughness dependence of thermal and electrical contact resistance. In: Proceedings of the 15th InterSociety Conference on Thermal and Thermomechanical Phenomena in Electronic Systems, ITherm 2016; jul. Institute of Electrical and Electronics Engineers Inc.; 2016. p. 1078–1082.

Appendix A. Figure Appendix

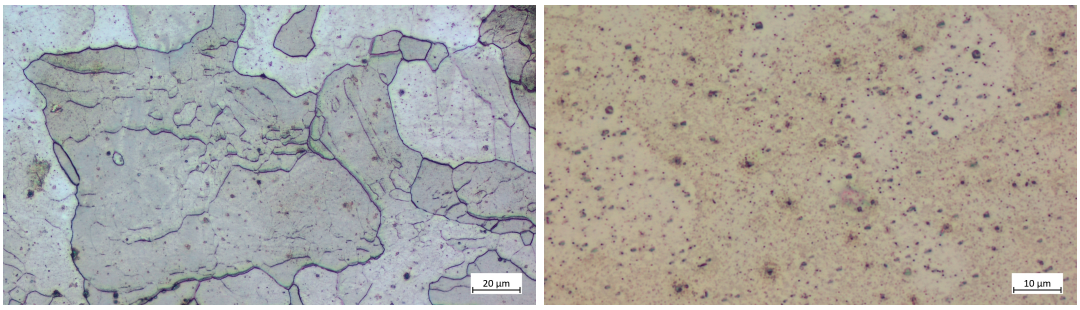

(a) As-Built (b) Heat-Treated

Figure A1.: Sample microstructure - high magnification
Alt text:"(a) As-Built: Microscopic image of a sample's microstructure at high magnification, showing large, irregularly shaped grains with clear boundaries. Some small pores and inclusions are visible within the grains.
(b) Heat-Treated: Microscopic image of a heat-treated sample's microstructure. It presents a more homogeneous appearance with a fine dispersion of tiny, dark spots throughout a lighter matrix, indicating a more uniform grain structure."

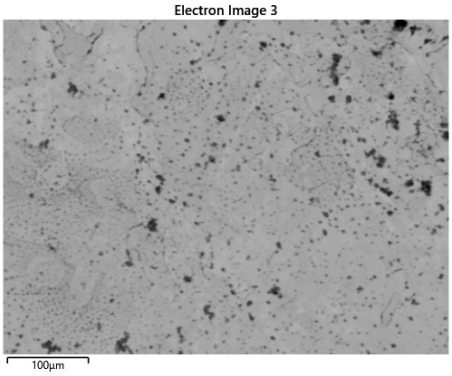

(a) SE

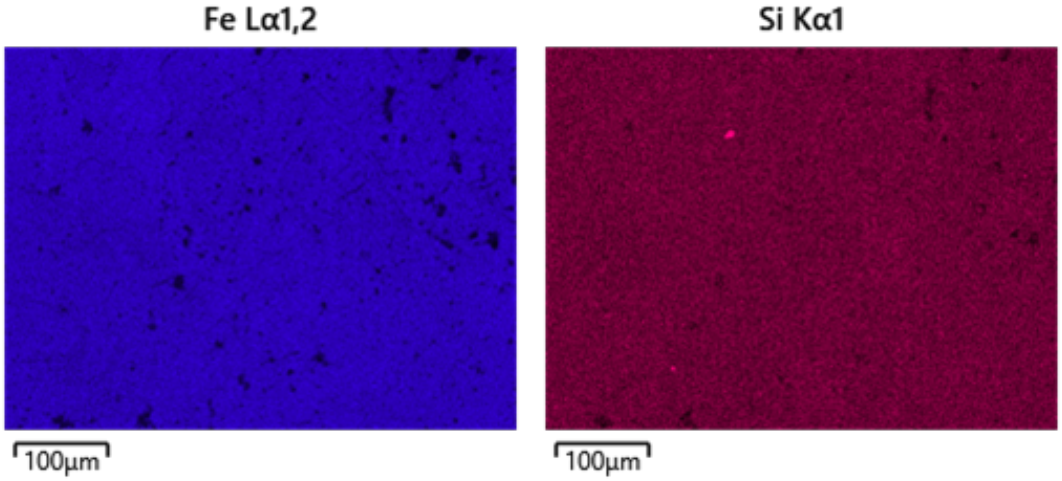

(b) BSE-FE

(c) BSE-SI

Figure A2.: BSE results for AsBuilt specimen

Alt text:"(a) SE: A grayscale secondary electron image showing a dense distribution of particles over a uniform background. Dark spots of various sizes are scattered throughout, indicating porosity or compositional variation.
(b) BSE-FE: A backscattered electron image highlighting the distribution of iron (Fe) in blue tones. Darker regions represent higher concentrations of iron, with the majority of the sample showing a consistent light blue background indicating a uniform iron distribution with some small, isolated patches of darker blue.
(c) BSE-SI: Another backscattered electron image representing the distribution of silicon (Si) in red tones. The image is almost uniform in color with a few specks of brighter intensity, suggesting a homogenous distribution of silicon with minimal variation or clustering."

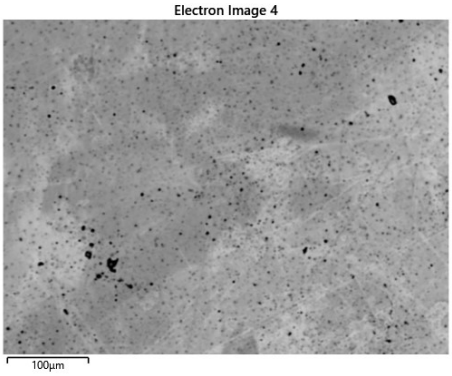

(a) SE

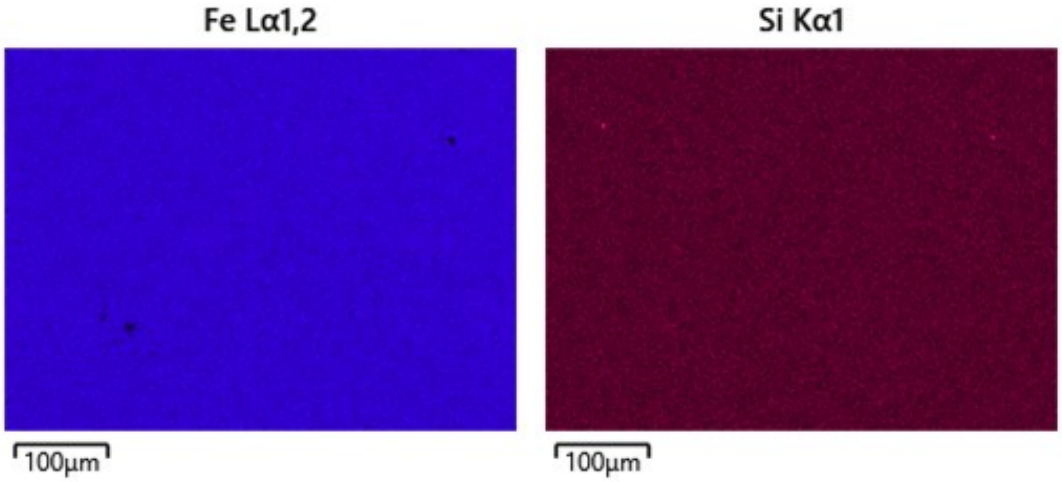

(b) BSE-FE

(c) BSE-SI

Figure A3.: BSE results for Heat Treated specimen

Alt text:"(a) SE: A grayscale image from a secondary electron detector displaying a relatively even distribution of fine particles across a uniform background. A few darker spots, indicating areas of higher topographical elevation or compositional differences, are sparsely scattered.
(b) BSE-FE: A backscattered electron image representing iron (Fe) distribution in deep blue. The consistent color across the image suggests a homogeneous distribution of iron with very few darker spots indicating concentrated areas.
(c) BSE-SI: Another backscattered electron image showing silicon (Si) distribution in a rich, uniform burgundy tone with no significant variation, indicating a consistent spread of silicon within the sample."

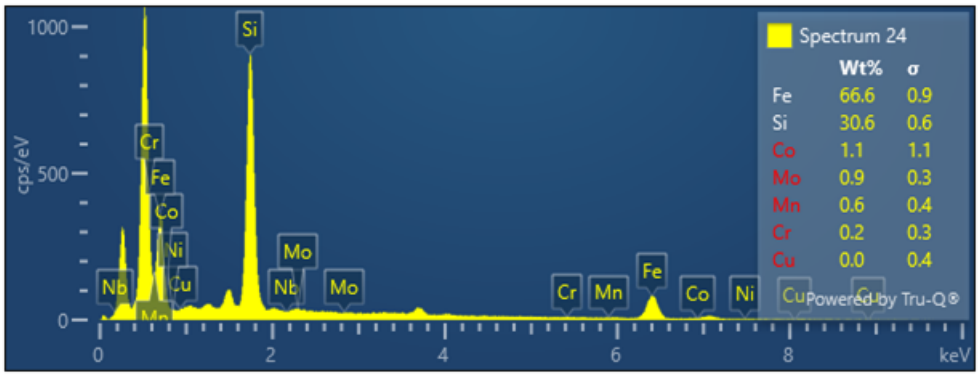

Figure A4.: Precipitate spectrum

Alt text:"EDS spectrum graph displaying peaks for various elements in a precipitate. Iron and silicon show the highest peaks, indicating a greater presence, while cobalt, molybdenum, and others are less prominent. A table details the weight percentages of each element."